Available online at www.sciencedirect.com
ScienceDirect
International Journal of Solids and Structures 44 (2007) 7975–7987
INTERNATIONAL JOURNAL OF SOLIDS AND STRUCTURES
www.elsevier.com/locate/ijsolstr

Subsurface initiated rolling contact fatigue of railway wheels as generated by rail corrugation

Anders Ekberg [a,*], Elena Kabo [a,b], Jens C.O. Nielsen [a], Roger Lundén [a]

[a] CHARMEC/Department of Applied Mechanics, Chalmers University of Technology, SE-412 96 Göteborg, Sweden
[b] Caran, Test & Analysis Department, Valdemar Noréns gata 3, SE-417 55, Göteborg, Sweden

Received 13 July 2006; received in revised form 28 March 2007
Available online 2 June 2007

Abstract

A fracture mechanics based fatigue index for rolling contact fatigue (RCF) initiated at deep (10–25 mm) defects is derived and employed together with a fatigue index for more shallow (4–10 mm) subsurface RCF initiation. Integrated simulations of high-frequency dynamic train–track interaction and prediction of RCF impact are then carried out to evaluate the influence of short-pitch rail corrugation on RCF of railway wheels. Parametric studies are carried out to identify operational conditions likely to generate high RCF impact. Simulation results show how rail corrugation causes a major increase in RCF impact at high-speed operations and that corrugation magnitudes measured in-field are sufficient to generate subsurface initiated RCF. At high speeds the main cause for increased fatigue impact is the increase in dynamic load magnitudes. At lower speeds and higher axle loads also the effect of poor contact geometry will have an influence.

Keywords: Rolling contact fatigue; High-frequency train–track interaction; Material defects; Rail corrugation; Wheel out-of-roundness; Numerical simulations

1. Introduction

In the years 1998 to 2002 a relatively large occurrence of subsurface initiated cracks due to RCF was detected in trailer wheels on Swedish high-speed trains. The number of detected cracks is now significantly reduced. A likely reason for this reduction is that rails are ground at more regular intervals, which reduces the magnitude of rail corrugation and roughness. The objective of the current study is to investigate the relationship between wheel and rail roughness and subsurface initiated RCF. The current paper extends a study by Nielsen et al. (2004) by focusing on RCF driving mechanisms. An accompanying paper (Nielsen et al., 2005) focuses on train–track dynamics aspects.

In the present paper an integrated study of train–track interaction and RCF is carried out. A wheel operating on a straight track with no long-wave geometrical defects (track irregularities) is considered.

* Corresponding author. Tel.: +46 31 772 3480; fax: +46 31 772 3827.
E-mail address: anders.ekberg@chalmers.se (A. Ekberg).

0020-7683/$ - see front matter © 2007 Elsevier Ltd. All rights reserved.
doi:10.1016/j.ijsolstr.2007.05.022

Wheel out-of-roundness is neglected in relation to the present rail irregularities. The running surface of the rail is corrugated, meaning that small amplitude undulations with a broad spectrum of wavelengths exist. The rail corrugation characteristics employed in the reference case are from measurements at a corrugated site (Vretstorp) by the Swedish National Rail Administration (Banverket). The studied roughness spectra include wavelengths in the interval 2–100 cm. This corresponds to excitation frequencies in the range 55–2778 Hz at a train speed of 200 km/h (the highest allowed speed at the site). Roughness levels are evaluated in a 1/3 octave band spectrum for centre wavelengths up to 31 cm. The roughness level is defined as

$$L_{\mathrm{r}} = 10 \cdot \log_{10}\left(\frac{\tilde{r}^2}{r_{\mathrm{ref}}^2}\right) \tag{1}$$

Here, $\tilde{r}$ [μm] is the root mean square value of the measured roughness profile and $r_{\mathrm{ref}} = 1$ μm.

Subsurface initiated rolling contact fatigue is assessed using the FIERCE model (Ekberg et al., 2002). The fast algorithms in FIERCE allow for fatigue evaluation in each time increment. This facilitates a statistical evaluation of the fatigue impact, which is of major importance in the study of RCF of railway wheels: Since the wheels are travelling along a track with varying characteristics, they will be subjected to a broad spectrum of fatigue loading. From a fatigue point of view, mainly extreme loads are of importance since, first, fatigue initiation is related to magnitudes of fatigue impact exceeding the (equivalent) fatigue limit and, second, above the fatigue limit life is decreasing exponentially with the increase in fatigue loading.

The current study focuses on fatigue impact in railway wheels owing to operations on corrugated rails. Naturally, this will also correspond to an increase in fatigue impact in the rails, of comparable magnitude. However, in rails phenomena such as global bending and global thermal contraction (in continuously welded rails) as well as boundary effects will have a more pronounced effect than in wheels. Note also that the effect of an out-of-round wheel will be similar to that of a corrugated rail with respect to RCF impact, see (Nielsen et al., 2005).

Finally, it is considered that the novelty of the current paper lies in the integration of high-frequency train–track interaction analysis and the refined RCF assessment to analyse the influence of rail roughness on subsurface initiated cracks; in that the primary causes of the high fatigue impact are investigated in depth, and in the evaluation of parametric influence.

2. Numerical models

2.1. Train–track interaction

The current study facilitates an integrated analysis of train–track interaction and rolling contact fatigue analysis. Train–track interaction is simulated in the time domain using the in-house code DIFF (Nielsen and Igeland, 1995). The DIFF-model incorporates high-frequency interaction up to some 2–3 kHz. It has been shown (Nielsen et al., 2004) that the high-frequency content is vital to obtain a good estimation of contact forces and fatigue impact for operations on corrugated rails. The issue is further explored in the accompanying paper (Nielsen et al., 2005), where it is concluded that, for the studied configurations there are large contributions to vertical contact loads in the frequency range 600–1200 Hz.

In the current study, the wheelset is modelled as a rigid mass supported by the primary suspension, which acts in longitudinal and vertical directions. Input data corresponding to existing powered and trailer wheelsets of a high-speed train are employed. Train speed and driving torque of the powered wheelset are assumed to be constant in each simulation to mimic steady-state conditions. The rail is modelled by the use of Rayleigh–Timoshenko finite beam elements. Sleepers are treated as rigid masses. A constant sleeper spacing of 0.63 m (c/c) is assumed. Track and loading properties (including the roughness profile) are taken as symmetric with respect to a centre line between the two rails. The length of the track model is 70 sleeper bays. Results are evaluated over a distance of 40 sleeper bays in the middle of the studied track section. Boundaries at the two rail ends are modelled as clamped. Rail pads and

ballast/underground in the discretely supported track model are modelled as two separate layers of linear springs and viscous dampers. Stiffnesses and viscous dampings were obtained by tuning the calculated vertical direct receptance of the railhead at sleeper midspan to the corresponding receptance measured at the test site Vretstorp. A nonlinear compressive stiffness of the wheel–rail contact is determined by assuming three-dimensional contact according to Hertz. Tangential wheel–rail contact is modelled using the Shen–Hedrick–Elkins friction law. The adopted procedure to simulate train–track interaction is described in detail in (Nielsen and Igeland, 1995). Details on the current model, including wheelset and track properties chosen to correspond to measured conditions, are available in (Nielsen et al., 2005) and (Nielsen et al., 2004).

3. Fatigue impact

3.1. Continuum based approach for subsurface fatigue initiation

To evaluate the risk of subsurface fatigue initiation, the Dang Van multiaxial fatigue criterion (Dang Van et al., 1989) is employed in the current study. The Dang Van equivalent stress, σ_{eq}, may be expressed as

$$\sigma_{eq} = \max_t(\tau_a(t) + c \cdot \sigma_h(t)) \tag{2}$$

Here, $\tau_a(t)$ is the time dependent magnitude of the deviation of the shear stress vector from its mid value during a stress cycle, $\sigma_h = (\sigma_x + \sigma_y + \sigma_z)/3$ is the hydrostatic stress, t is time and c is a material parameter. Fatigue initiation is predicted for $\sigma_{eq} > \tau_e$, where τ_e is the fatigue limit in shear of the material. It should be noted that τ_e may be significantly reduced by the presence of material defects, (cf. Ekberg and Marais, 2000; Ekberg and Sotkovszki, 2001; Kabo, 2002; Kabo and Ekberg, 2002a,b; Kabo and Ekberg, 2005). A reasonable estimation of a reduced fatigue limit under current conditions is $\tau_{e,red} \approx 220$ MPa, (cf. Ekberg and Sotkovszki, 2001). In addition, a rough estimation of expected fatigue life in cases of subsurface initiated fatigue may be obtained from an "equivalent S–N-curve" which relates the magnitude of the Dang Van equivalent stress to the fatigue life, see (Ekberg, 1997).

For analysis of subsurface initiated rolling contact fatigue of wheels and rails under Hertzian contact conditions, an approximation of the Dang Van equivalent stress (Ekberg et al., 2002; Ciavarella and Maitournam, 2004; Ekberg et al., 2004) may be expressed as

$$FI_{sub} \equiv \sigma_{eq} \approx \frac{F_z}{4\pi ab}(1 + f^2) + c \cdot \sigma_{h,res} \tag{3}$$

where a and b are the semi-axes of the elliptical wheel–rail contact patch, F_z is the load acting normal to the contact area, and $f = \sqrt{(F_x^2 + F_y^2)}/F_z$ is the traction coefficient with F_x and F_y being tangential loads on the wheel tread acting in circumferential and transverse directions, respectively. Further, c is a material parameter and $\sigma_{h,res}$ the hydrostatic part of the residual stress in the wheel.[1] The error in the approximative expression in Eq. (3) as compared to a thorough evaluation of the Dang Van stress is less than some 8% for the current application, see (Ekberg et al., 2002).

3.2. Fracture mechanics based approach

The Dang Van equivalent stress is of relevance for rolling contact fatigue cracks initiated at a depth of some 5–10 mm below the wheel tread. For cracks initiated deeper, say down to some 25 mm, the influence of material defects becomes even more important since nominal stress magnitudes are low. For such deep cracks, the contact geometry is of less importance and the fatigue impact is better reflected by the contact load magnitude, F_z, (see Ekberg et al., 2002; Kabo, 2002; Kabo and Ekberg, 2002a,b; Kabo and Ekberg, 2005). Elasto-plastic simulations (Lansler et al., 2006) have further shown that linear elastic fracture mechanics is likely to be valid

[1] Compressive (negative) residual stresses should here be treated with caution. From experiments it has been found that they do not have the beneficial effect predicted by the Dang Van criterion (Desimone et al., 2006). It is therefore advisable to use $\sigma_{h,res} = 0$ in the presence of compressive residual stresses.

and that mode I crack opening does not occur for the current case of a relatively deep crack. Consequently, ΔK_{II} should here be a suitable measure of fatigue loading.

3.2.1. Two-dimensional approach

Presuming elastic plain strain (2D) conditions, that the contact load may be approximated as a line load, that the crack is relatively short, and that there is slip between the crack faces, the mode II stress intensity factor of a crack parallel to the contacting surface may be expressed as (Hearle and Johnson, 1985)

$$K_{II} = -\frac{2F_z}{\pi h}\cdot\sqrt{\frac{\pi L}{2}}\left(\frac{x}{h}+\mu\right)\left(\frac{1+\frac{f\cdot x}{h}}{\left(1+\left(\frac{x}{h}\right)^2\right)^2}\right) \tag{4}$$

where F_z is the magnitude of the line load, h is the depth of the crack below the surface, L the length of the crack, x the lateral distance between the crack centre and the applied load and μ the crack face friction coefficient.

If the wheel–rail contact is traction free, i.e. $f = 0$, Eq. (4) may be simplified to

$$K_{II} = -\frac{2F_z h^2}{\pi}\cdot\sqrt{\frac{\pi L}{2}}\left(\frac{x+\mu h}{(h^2+x^2)^2}\right) \tag{5}$$

Extreme magnitudes of K_{II} will for this case occur for

$$x = \frac{h}{3}\left(\pm\sqrt{3+4\mu^2}-2\mu\right) \tag{6}$$

and have a magnitude of

$$K_{II,\max} = \frac{27F_z}{8h}\cdot\sqrt{\frac{L}{2\pi}}\cdot\frac{\left(-\mu+\sqrt{3+4\mu^2}\right)}{\left(3+2\mu^2+\mu\sqrt{3+4\mu^2}\right)^2} \tag{7}$$

If also crack face friction is neglected, i.e., $\mu = 0$, extreme magnitudes of K_{II} will occur at

$$x = \pm\frac{h}{\sqrt{3}} \tag{8}$$

and have a magnitude of

$$K_{II,\max} = \frac{3F_z}{8h}\cdot\sqrt{\frac{3L}{2\pi}} \tag{9}$$

Neglecting the effect of crack face friction may, based on elastic simulations (Hearle and Johnson, 1985), be considered as a too conservative simplification. However, elasto-plastic simulations indicate that the influence of crack face friction may be less in practise (Lansler et al., 2006). Further, subsurface cracks often appear in the presence of MnS-inclusions, which will tend to lubricate the crack faces. Finally it may be noted that operational magnitudes of crack face friction typically are unknown and very cumbersome to measure or estimate.

Since the evolution of K_{II} is anti-symmetric with respect to the load position, we will for cases of friction free crack face contact obtain the mode II stress intensity range as

$$\Delta K_{II} = 2\cdot K_{II,\max} = \frac{3F_z}{4h}\cdot\sqrt{\frac{3L}{2\pi}} \tag{10}$$

Fig. 1 shows the evolution of stress intensity factors evaluated at the leading (K_L; the first crack tip to be loaded) and trailing (K_T) crack tips and evaluated under the presumption of a uniform shear stress over the crack length (short crack). The maximum magnitude of K_{II} according to Eqs. (8) and (9) is indicated by a ring in Fig. 1.

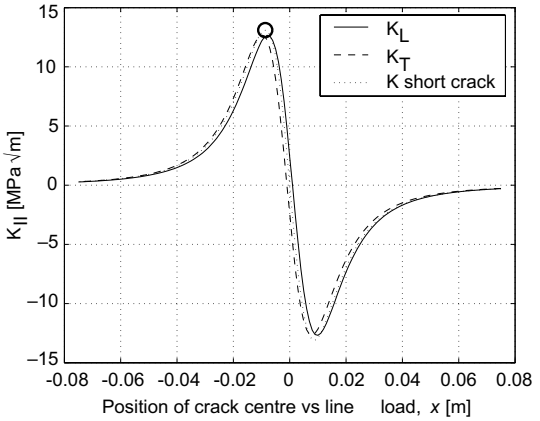

Fig. 1. Evolution of stress intensity factor K_{II} at a crack ($h = 15$ mm, $L = 4$ mm) owing to a passing line load of 12 MN/m. Peak value according to Eqs. (8) and (9) is indicated by a circle. Two-dimensional plane strain is assumed.

3.2.2. Three-dimensional approach

If crack face friction is neglected, the largest (along the crack face) mode II stress intensity factor of a penny-shaped crack[2] in an infinite body subjected to a uniform shear, τ, may be expressed as (Murakami, 1990; Kassir and Sih, 1966)

$$K_{II} = \frac{4\sqrt{r}}{(2-\nu)\cdot\sqrt{\pi}}\cdot\tau \tag{11}$$

Here, ν is the Poisson ratio and r the radius of the penny-shaped crack, cf Fig. 2.

In a semi-infinite body subjected to a point load, F_z, the shear stress at a material point in the plane $y = 0$ according to 2 may be expressed as (Kannel and Tevaarwerk, 1984)

$$\tau_{xz} = \frac{3xh^2}{2\pi(\sqrt{x^2+h^2})^5}\cdot F_z \tag{12}$$

A combination of Eqs. (11) and (12) yields

$$K_{II} = \frac{6\sqrt{r}}{(2-\nu)\cdot\pi\sqrt{\pi}}\cdot\frac{xh^2}{(\sqrt{x^2+h^2})^5}\cdot F_z \tag{13}$$

As the point-load moves along the x-axis, extreme magnitudes of K_{II} will occur for

$$x_{max} = \pm h/2 \tag{14}$$

and the maximum magnitude will be

$$K_{II,max} = \frac{96}{25\sqrt{5}\cdot(2-\nu)\cdot\pi\sqrt{\pi}}\cdot\frac{\sqrt{r}}{h^2}\cdot F_z \tag{15}$$

Fig. 3 shows the evolution of K_{II} according to Eq. (13) with maximum magnitudes according to Eqs. (14) and (15) marked by a filled circle.

Owing to the anti-symmetric evolution, the mode II stress intensity factor range will be

$$\Delta K_{II} = 2\cdot K_{II,max} = \frac{192}{25\sqrt{5}\cdot(2-\nu)\cdot\pi\sqrt{\pi}}\cdot\frac{\sqrt{r}}{h^2}\cdot F_z \tag{16}$$

[2] The more general case of an elliptic crack (also covered by given references) is studied by Beretta et al. (2001).

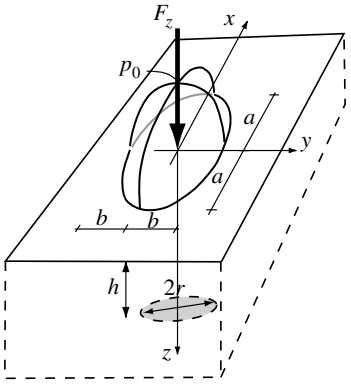

Fig. 2. A penny-shaped crack of radius r located at a depth h below the contact surface. The crack is subjected to a Hertzian contact pressure with peak magnitude p_0, in the current study approximated by the resultant point load F_z.

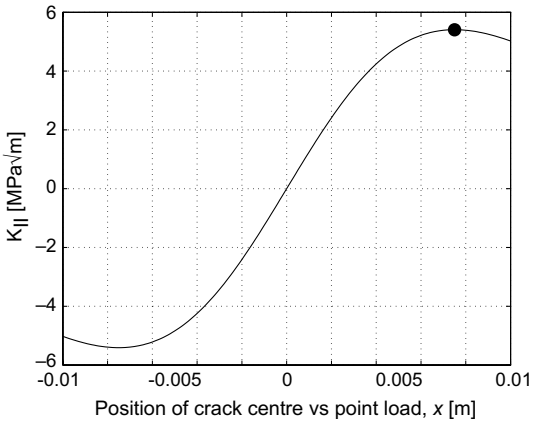

Fig. 3. Evolution of K_{II} for a penny-shaped crack ($r = 2$ mm, $h = 15$ mm) and loaded by a moving compressive point load of $F_z = 150$ kN. Maximum magnitude of K_{II} as given by Eqs. (14) and (15) is indicated by a filled circle.

According to the theory of linear elastic fracture mechanics, the fatigue crack is predicted to grow if $\Delta K_{II} > \Delta K_{II,th}$ where $\Delta K_{II,th}$ is a material parameter. Further, if a Paris type of evolution law is presumed to be valid, the crack growth rate, da/dN, will be given by

$$\frac{da}{dN} = C_{II}(\Delta K_{II})^{m_{II}} \tag{17}$$

where C_{II} and m_{II} are material parameters. In evaluating the fatigue impact for certain operational conditions the crack configuration is often unknown. To circumvent this, we study a given configuration where h and r are constant and introduce the normalised measure

$$FI_{cra} \equiv \frac{h^2}{\sqrt{r}} \cdot \Delta K_{II} = \frac{192}{25\sqrt{5} \cdot (2-\nu) \cdot \pi\sqrt{\pi}} \cdot F_z \tag{18}$$

which will be used in the following to quantify the fatigue impact at deep cracks. In particular we note that $\Delta K_{II} \propto F_z$.

In cases of line-like contacts, e.g. roller bearings, a similar criterium based on ΔK_{II} as outlined in Section 3.2.1 should be more accurate.

4. Parametric influences

As mentioned above, the magnitudes of FI_{sub} and FI_{cra} according to Eqs. (3) and (18), will reflect the fatigue impact, i.e. the fatigue loading of the material. To predict whether fatigue will initiate in the material and, in such a case, the component's fatigue life requires also a knowledge of the material's fatigue strength. However, this issue is not studied in the following. Instead the focus is on the influence of operational parameters on the fatigue impact. Magnitudes of FI_{sub} and FI_{cra} in the following should thus be taken as indicators of the risks of fatigue initiation and/or expected fatigue lives.

If nothing else is stated, parameters correspond to the reference case with an axle load of 12 tonnes of which 1390 kg corresponds to the unsprung mass; a speed of 200 km/h and a roughness level as corresponding to field measurements described in Nielsen et al. (2005). Input data to the track model are listed in Nielsen et al. (2005). Probability densities, p, are derived according to the formula

$$p = \frac{n}{\Delta \cdot N} \tag{19}$$

where n is the number of time increments corresponding to a fatigue index magnitude within a given interval, N is the total number of intervals, and Δ width of each interval.

4.1. Axle load and unsprung wheel mass

An increased axle load will increase the fatigue impact in terms of average magnitudes of FI_{sub} and FI_{cra}. For FI_{sub}, the scatter will decrease with increased axle load, which makes the difference between extreme magnitudes of FI_{sub} less than that of average magnitudes as seen in Fig. 4. Since fatigue initiation and subsequent fatigue crack growth are to a large extent threshold problems, it is the extreme magnitudes of FI_{sub} that are most important. Consequently, the influence of an increased axle load on shallowly initiated subsurface RCF (as quantified by FI_{sub}) is not as severe as on deep cracks (as quantified by FI_{cra}). It should here be noted that the case of an axle load of 6 tonnes operating on a corrugated track at 200 km/h introduces loss of contact at several instances in time. For such conditions FI_{sub} is undefined since both F_z and ab are zero. These occasions have not been included in Fig. 4a.

In Fig. 5 it is seen that a change in unsprung wheel mass will not significantly affect neither FI_{sub} nor FI_{cra} provided the total axle load is kept constant.

In summary, an increased axle load is of importance to fatigue impact, especially to the initiation of deep cracks as reflected by the magnitude of FI_{cra}. However, for the studied cases, the increase in fatigue impact is not related to whether the increase in axle load is unsprung or not.

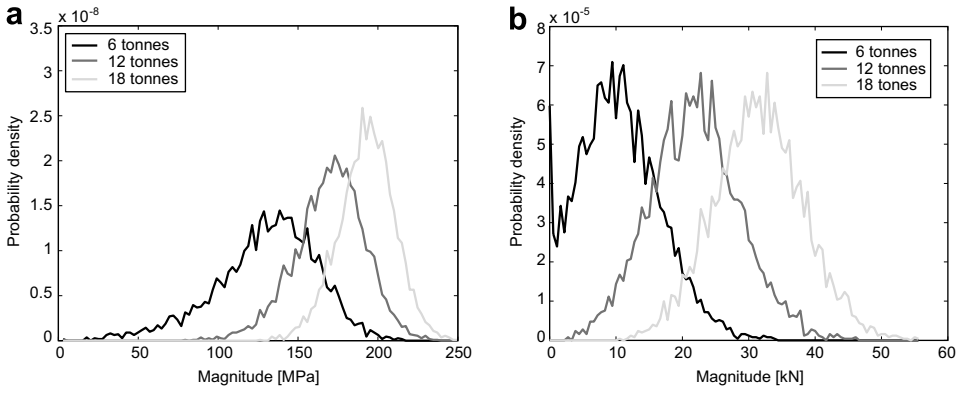

Fig. 4. Influence of axle load: 6 tonnes, 12 tonnes (reference case) and 18 tonnes. FI_{sub} (left) FI_{cra} (right).

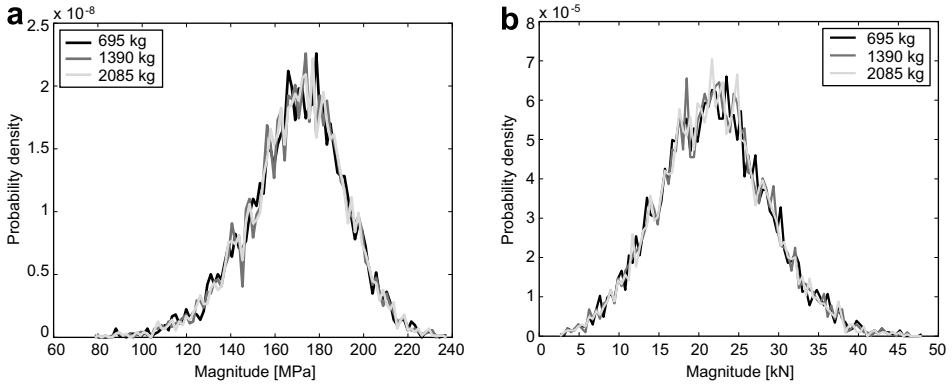

Fig. 5. Influence of unsprung mass: 695 kg, 1390 kg (reference case) and 2085 kg. Total axle load is 12 tonnes for all cases. FI_{sub} (a) FI_{cra} (b).

4.2. Roughness level

The influence of rail roughness on the fatigue impact has been investigated by analysing four magnitudes of rail corrugation. The reference case corresponds to corrugation magnitudes measured at the Vretstorp test site (Nielsen et al., 2005). In addition, cases for which this corrugation spectrum has been decreased by 3 or 6 dB or increased by 3 dB according to Eq. (1) have been simulated. A case where the roughness was increased by 6 dB led to severe loss of contact and was excluded from the study.

As can be seen from Fig. 6, an increased roughness level will increase the scatter of both FI_{sub} and FI_{cra}. Consequently, the maximum magnitudes will increase which implies a higher probability of RCF initiation and decreased RCF lives for both deep and shallow cracks.

4.3. Operational speed

The influence of train speed is shown in Fig. 7. It can be seen that an increased speed will have a similar effect as an increased roughness level in that scatter, and thus extreme magnitudes of both FI_{sub} and FI_{cra}, are increased.

Of interest is the "saturation effect" in the sense that an increase in speed from 100 km/h to 200 km/h gives a much higher increase in peak fatigue impacts (in terms of both FI_{sub} and FI_{cra}) than an increase from 200 km/h to 300 km/h.

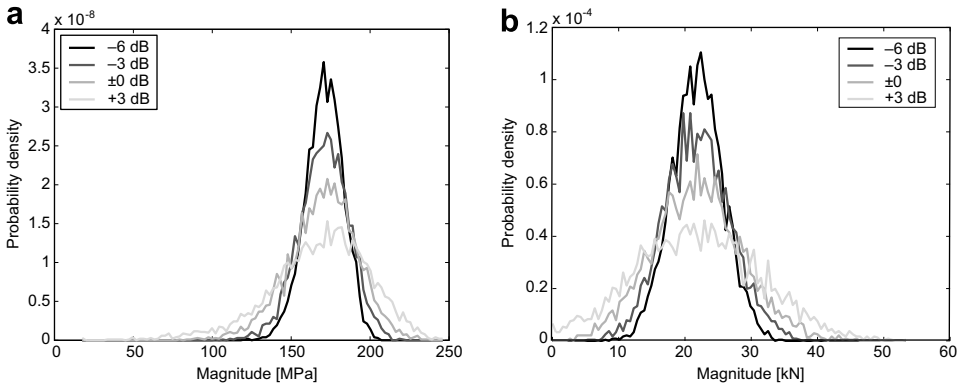

Fig. 6. Influence of roughness level. Reference case and roughness increased by 3 dB or decreased by 3 dB or 6 dB according to Eq. (1). FI_{sub} (a) FI_{cra} (b).

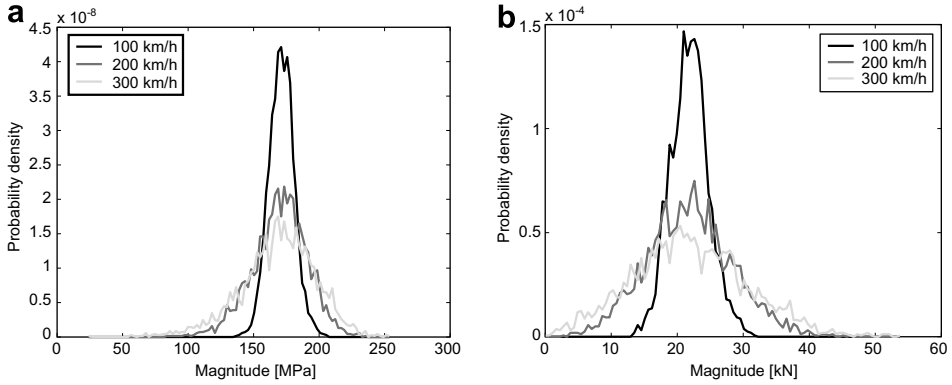

Fig. 7. Influence of train speed: 100 km/h, 200 km/h (reference case) or 300 km/h. FI_{sub} (a) FI_{cra} (b).

5. Causes of high fatigue impact

5.1. Vertical contact load versus contact geometry

In Fig. 8 the vertical contact load, F_z, is plotted versus the contact geometry, as measured by the product of Hertzian contact patch semi-axes $a \cdot b$. The load cases (time increments) corresponding to the 25 highest magnitudes of FI_{sub} are marked with black squares. A "high" corrugation level, c, here corresponds to magnitudes as measured at the test site Vretstorp and a low magnitude corresponds to a 50% roughness reduction.

It is seen that a high magnitude of FI_{sub} strongly correlates to a high magnitude of F_z. An exception is the case of low-speed operations (Fig. 8d), where a high FI_{sub} magnitude at some occasions corresponds to a relatively low vertical load F_z.

5.2. Contact geometry

In Fig. 9, the contact semi-axis b is plotted versus the semi-axis a. Here, a corresponds to the direction along the rail. The 25 most damaging load cases (time increments) are marked with black squares. It should be noted that the roughness is modelled as one-dimensional, i.e. the irregularities are modelled in the rail direction (corresponding to the semi-axis a) and the profile is assumed constant in the transverse direction (corresponding to the semi-axis b). It can be seen that a high FI_{sub} always corresponds to a large value of b, owing to the high load level. As for the semi-axis a, the trend is more complicated. Typically, a high FI_{sub} corresponds to a fairly large a-value, but there are exceptions, most notably low-speed and heavy operations. Low a magnitudes correspond either to a low F_z (resulting in a low FI_{sub}) or to a poor contact geometry, e.g. when the wheel traverses the corrugation peaks. The latter case may result in high FI_{sub} magnitudes.

6. Conclusions

A previously developed analytical expression for the subsurface Dang Van stress in railway wheels (Ekberg et al., 2002) has been complemented by an analytical expression for ΔK_{II} of a deep crack subjected to a passing contact load. These two indices, FI_{sub} and FI_{cra}, have been adopted to evaluate the rolling contact fatigue impact regarding subsurface initiated cracks in railway wheels.

It can be concluded that corrugation will increase rolling contact fatigue impact. The underlying mechanisms are as follows:

- The roughness of the rail surface will lead to increased contact load magnitudes due to its influence of the dynamic train–track interaction. This is the dominating cause of high fatigue impact in high-speed operations.

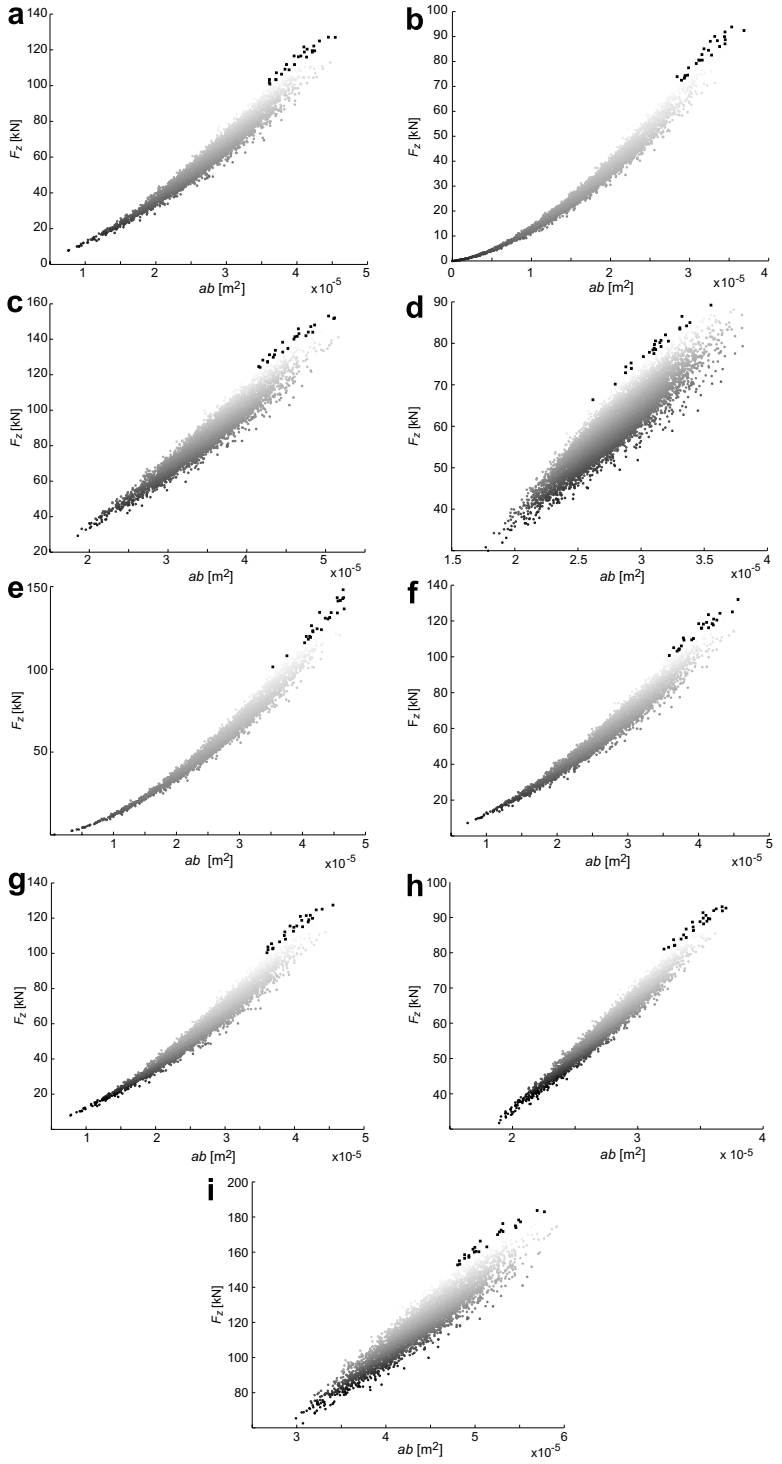

Fig. 8. Scatter plot of F_z vs $a \cdot b$. The 25 highest magnitudes of FI_{sub} are marked with black squares. Please note the variation in scales. Speed, v, axle load, V, unsprung mass, M, and corrugation level, c, are: (a) $v = 200$ km/h, $V = 12$ tonnes, $M = 1390$ kg, c high (b) $v = 200$ km/h, $V = 6$ tonnes, $M = 1390$ kg, c high (c) $v = 200$ km/h, $V = 18$ tonnes, $M = 1390$ kg, c high (d) $v = 100$ km/h, $V = 12$ tonnes, $M = 1390$ kg, c high (e) $v = 300$ km/h, $V = 12$ tonnes, $M = 1390$ kg, c high (f) $v = 200$ km/h, $V = 12$ tonnes, $M = 695$ kg, c high (g) $v = 200$ km/h, $V = 12$ tonnes, $M = 2085$ kg, c high (h) $v = 200$ km/h, $V = 12$ tonnes, $M = 1390$ kg, c low (i) $v = 200$ km/h, $V = 25$ tonnes, $M = 1390$ kg, c high.

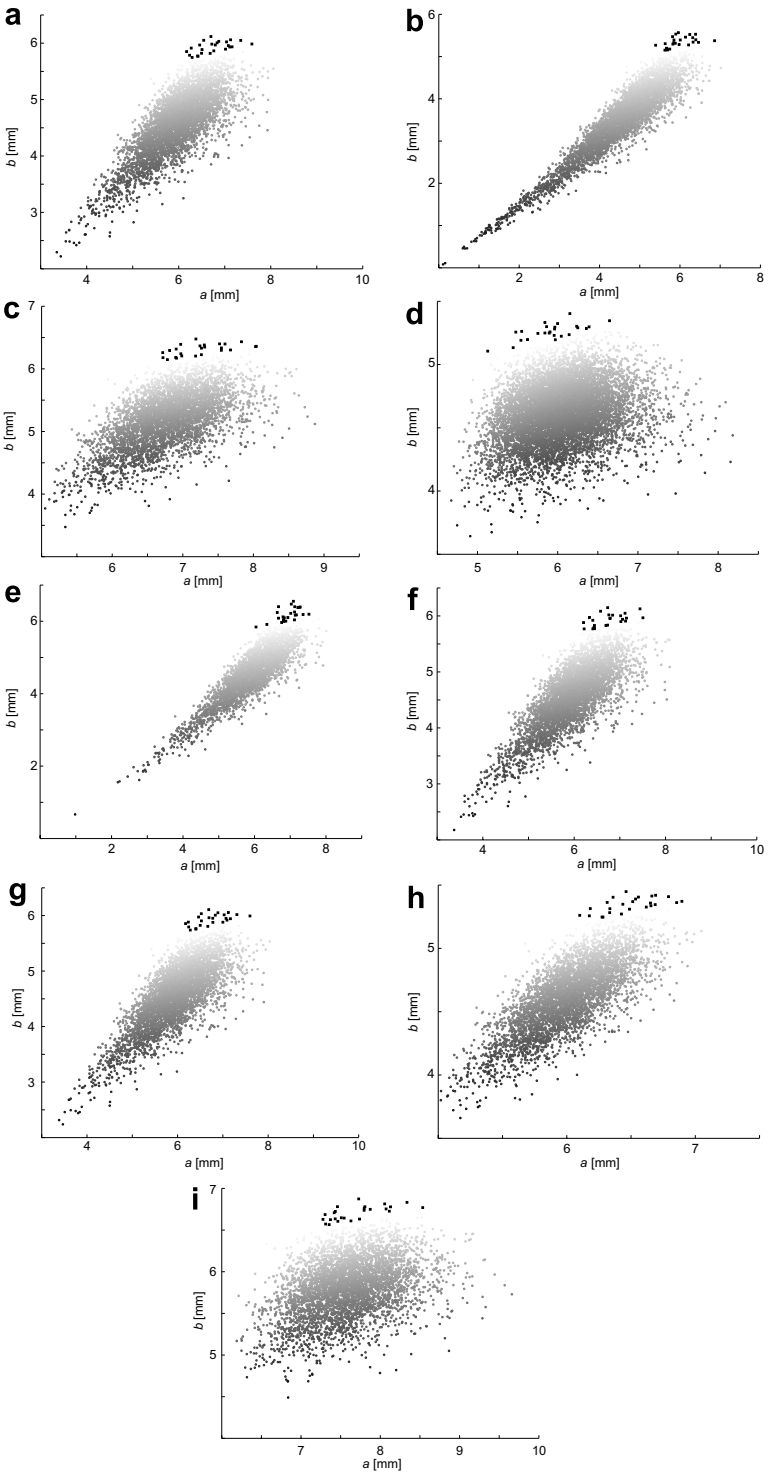

Fig. 9. Scatter plot of contact semi-axis b vs a. Combinations corresponding to the 25 highest magnitudes of FI_{sub} are marked with black squares. Speed, v, axle load, V, unsprung mass, M, and corrugation level, c, are: (a) $v = 200$ km/h, $V = 12$ tonnes, $M = 1390$ kg, c high (b) $v = 200$ km/h, $V = 6$ tonnes, $M = 1390$ kg, c high (c) $v = 200$ km/h, $V = 18$ tonnes, $M = 1390$ kg, c high (d) $v = 100$ km/h, $V = 12$ tonnes, $M = 1390$ kg, c high (e) $v = 300$ km/h, $V = 12$ tonnes, $M = 1390$ kg, c high (f) $v = 200$ km/h, $V = 12$ tonnes, $M = 695$ kg, c high (g) $v = 200$ km/h, $V = 12$ tonnes, $M = 2085$ kg, c high (h) $v = 200$ km/h, $V = 12$ tonnes, $M = 1390$ kg, c low (i) $v = 200$ km/h, $V = 25$ tonnes, $M = 1390$ kg, c high.

- The roughness will also promote a poor contact geometry (small contact patch). This effect is counter-acted by the higher contact loads that tend to increase the size of the Hertzian contact patch. This interaction can be seen by studying the relation between the contact patch semi-axes a and b. The b-measure is not directly affected by the roughness (since the roughness is here taken as one-dimensional), whereas a-measures are affected. For low speeds, the dynamic increase of F_z is not sufficient to exceed the effect of a small contact patch, as can be seen by the relatively lower magnitudes of a for load cases corresponding to high magnitudes of FI_{sub} in low-speed operations. For extreme low-speed operations, the poor contact geometry owing to the corrugation will be the main cause to an increased fatigue impact (as understood by considering the quasi-static case). For higher speeds, the effect of an increased magnitude of F_z will exceed the influence of the corresponding increase in the size of the Hertzian contact patch. Consequently a high fatigue impact is here related to high contact load magnitudes and large contact patches.
- Higher axle loads will increase RCF impact, in particular with respect to deep cracks.
- Higher axle loads also causes a larger spread in contact geometries. A plausible explanation is that the high load tends the wheel to roll more closely along the troughs and peaks of the corrugated rail.
- An increase in unsprung mass will have no effect on fatigue impact providing the static axle load is not affected. The reason is likely to be that at the high load frequencies imposed by the corrugation, the mass of the wheel can be seen as infinite.
- For the operational conditions studied, corrugation is more of an issue in high speed operations as compared to heavy haul. This is in line with operational experience.

Acknowledgement

The current work is part of the activities within CHARMEC, see www.charmec.chalmers.se.

References

Beretta, S., Donzella, G., Roberti, R., Ghidini, A., 2001. Deep shelling in railway wheels. in: Proceedings 13th International Wheelset Congress, Rome, Italy.

Ciavarella, M., Maitournam, H., 2004. On the Ekberg, Kabo and Andersson calculation of the Dang Van high cycle fatigue limit for rolling contact fatigue. Fatigue & Fracture of Engineering Materials & Structures 27 (6), 523–526.

Dang Van, K., Cailletaud, G., Flavenot, J.F., Le Douaron, A., Lieurade, H.P., 1989. Criterion for high cycle fatigue failure under multiaxial loading. Biaxial and multiaxial fatigue. Mechanical Engineering Publications, London, UK, pp. 459–478.

Desimone, H., Bernasconi, A., Beretta, S., 2006. On the application of Dang Van criterion to rolling contact fatigue. Wear 260 (4–5), 567–572.

Ekberg, A., 1997. Rolling contact fatigue of railway wheels – a parametric study. Wear 211 (2), 280–288.

Ekberg, A., Kabo, E., Andersson, H., 2002. An engineering model for prediction of rolling contact fatigue of railway wheels. Fatigue & Fracture of Engineering Materials & Structures 25 (10), 899–909.

Ekberg, A., Kabo, E., Andersson, H., 2004. Answer to the letter to the editor by M Ciavarella and H Maitournam. Fatigue & Fracture of Engineering Materials & Structures 27 (6), 527–528.

Ekberg, A., Marais, J., 2000. Effects of imperfections on fatigue initiation in railway wheels. IMechE Journal of Rail and Rapid Transit 214 (F1), 45–54.

Ekberg, A., Sotkovszki, P., 2001. Anisotropy and rolling contact fatigue of railway wheels. International Journal of Fatigue 23 (1), 29–43.

Hearle, A.D., Johnson, K.L., 1985. Mode II stress intensity factors for a crack parallel to the surface of an elastic half-space subjected to a moving point load. Journal of the Mechanics and Physics of Solids 33 (1), 61–81.

Kabo, E., 2002. Material defects in rolling contact fatigue of railway wheels – influence of overloads and defect clusters. International Journal of Fatigue 24 (8), 887–894.

Kabo, E., Ekberg, A., 2002a. The influence of defects in rolling contact fatigue. In: Proceedings of Rolling Contact Fatigue: Applications and Developments, Brescia, Italy.

Kabo, E., Ekberg, A., 2002b. Fatigue initiation in railway wheels – a numerical study of the influence of defects. Wear 253 (1–2), 26–34.

Kabo, E., Ekberg, A., 2005. Material defects in rolling contact fatigue of railway wheels – the influence of defect size. Wear 258 (7–8), 1194–1200.

Kannel, J.W., Tevaarwerk, J.L., 1984. Subsurface stress evaluations under rolling/sliding contacts. Journal of Tribology 106 (1), 96–103.

Kassir, M.K., Sih, G.C., 1966. Three-dimensional stress distribution around elliptical crack under arbitrary loadings. Journal of Applied Mechanics 33 (3), 601–611.

Lansler, E., Ekberg, A., Kabo, E., Andersson, H., 2006. Influence of plastic deformations on growth of subsurface rolling contact fatigue cracks in railway wheels. IMechE Journal of Rail and Rapid Transit 220 (F4), 461–473.

Murakami, Y., 1990. In: Stress intensity factors handbook, vol. 2. Pergamon Press, Oxford, UK, pp. 686–689.

Nielsen, J.C.O, Ekberg, A., Kabo E., Lundén, R., 2004. Integrated analysis of dynamic train–track interaction and rolling contact fatigue. In: Proceedings of the International Wheelset Congress 2004, Orlando, USA.

Nielsen, J.C.O., Ekberg, A., Lundén, R., 2005. Influence of short-pitch wheel/rail corrugation on rolling contact fatigue. IMechE Journal of Rail and Rapid Transit 219 (F3), 177–187.

Nielsen, J.C.O., Igeland, A., 1995. Vertical dynamic interaction between train and track – influence of wheel and track imperfections. Journal of Sound and Vibration 187 (5), 825–839.